RSC Advances

PAPER

View Article Online
View Journal | View Issue

Cite this: *RSC Adv.*, 2017, **7**, 16678

N-Doped hierarchical porous carbon from waste boat-fruited sterculia seed for high performance supercapacitors†

Wenxiu Wang,[ab] Hongying Quan,*[a] Weimin Gao,[b] Ren Zou,[b] Dezhi Chen,*[b] Yinghu Dong[a] and Lin Guo*[bc]

N-Doped hierarchical porous carbon (NHPC) was obtained from waste boat-fruited sterculia seed by hydrothermal carbonization and KOH activation. The influence factors including the ratio of activation agent to precursor, activation temperature, and heteroatom-doping were discussed. The results showed that the NHPC-800-1 activated at 800 °C with the ratio of activation agent to precursor being 1 as an electrode in an electrical double layer capacitor (EDLC) exhibited the best electrochemical performance in 6 M KOH electrolyte. It delivered the specific capacitance up to 337 F g^{-1} at a current density of 1 A g^{-1}, and still retained a capacitance of 181.5 F g^{-1} at the high current density of 50 A g^{-1}. This material also shows an excellent capacitance retention of 98.8% after 5000 cycles at a current density of 20 A g^{-1}. In addition, a symmetric supercapacitor fabricated by NHPC-800-1 released an energy density of 8.05 W h kg^{-1} at a power density of 10 kW kg^{-1}, and a high cycling stability with a capacitance retention of 98.5% over 10 000 cycles at 20 A g^{-1} in 6 M KOH electrolyte. The superior performance of NHPC-800-1 could be attributed to these advantages of hierarchical porous structure, narrow micropore size distribution and rational micro/mesopore ratio, as well as the doping of the N atoms. These very attractive electrochemical properties indicate that the NHPC-800-1 derived from boat-fruited sterculia is a promising electrode material for supercapacitors.

Received 24th January 2017
Accepted 6th March 2017

DOI: 10.1039/c7ra01043e

rsc.li/rsc-advances

Introduction

Electrochemical capacitors, also called supercapacitors, which combine the advantages of both dielectric capacitors that can deliver high power within a very small period and rechargeable batteries that store high energy density, are currently considered as one of the most promising energy storage and power supply devices for electric vehicles, portable electronics, and uninterruptible or emergency power supplies.[1–5] Depending on the energy storage mechanism, supercapacitors can be divided into two categories: electrical double layer capacitors (EDLCs), which store energy based on pure electrostatic attraction between ions and the charged surface of an electrode,[6] such as carbon materials;[7–11] and pseudo-capacitors which store energy by fast and reversible oxidation/reduction (redox) or faradaic charge transfer reactions of the electro-active materials, for example, transition metal oxides,[12–18] transition metal hydroxides,[19] and conductive polymers.[20–23] The properties of the electrode have a very important influence on the electrochemical properties of supercapacitors. Therefore, it is very important to develop high performance electrode materials for fundamental advances in supercapacitor application.

In the field of supercapacitors, carbon materials are the most commonly electrode materials due to their advantages of high electrical conductivity, high surface area, pore volume and electrochemical stability.[24–26] Up to date, available carbon materials used for supercapacitors electrode include activated carbons,[27] carbon quantum,[28] carbon nanofibers,[29] carbon nanotubes[30,31] and graphene.[32] Among these carbon materials, activated carbons are a type of good candidate because they are commercially available and cheap, and can be produced from renewable biomass. However, supercapacitors based on common activated carbons with low specific capacitance, especially at the high charge/discharge current density, have limited the practical use of activated carbons.[33]

Many efforts have used to improve supercapacitor performance of activated carbons such as designing novel structures, constructing hierarchical pore architecture as well as introducing defects and heteroatom and/or functional groups.[26,29,33–36] Novel

[a]School of Materials Science and Engineering, Nanchang Hangkong University, Nanchang 330063, China. E-mail: quanhongying@nchu.edu.cn

[b]Key Laboratory of Jiangxi Province for Persistent Pollutants Control and Resources Recycle, School of Environmental and Chemical Engineering, Nanchang Hangkong University, Nanchang 330063, China. E-mail: chendz@nchu.edu.cn; guolin@buaa.edu.cn

[c]Key Laboratory of Bio-Inspired Smart Interfacial Science and Technology of Ministry of Education, School of Chemistry and Environment, Beihang University, Beijing 100191, China

† Electronic supplementary information (ESI) available. See DOI: 10.1039/c7ra01043e

structures can effectively shorten the pathways of ions diffusion and offer minimized diffusive resistance to mass transport on the interface between electrode and electrolyte.[37–39] Hierarchical pore architecture with an interconnected macro-, meso-, and microporous network can accelerate the speed of ion transport with improved rate capability.[27,37,40,41] In addition, the doping of heteroatom such as O, N, S and F not only can increase available active sites, but also effectively improve their surface wettability, electric conductivity and capacitance properties.[33,42–45] Compared with any one of above-mentioned approaches, it is no doubt that the multiple synergistic effects of these approaches will more efficiently promote the electrochemical performance of activated carbon used as electrodes of supercapacitor.[33,36,46,47] Recently, by selecting appropriate biomass and synthetic routes, novel activated carbon materials with hierarchical pore architecture and the doping of heteroatom can be prepared,[35–37,39,46,48–51] and have exhibited excellent electrochemical performance as electrode materials in EDLCs.

Boat-fruited sterculia seed (Semen Sterculiae Lychnophorae) is a tropical herb of the sterculiaceae family, mainly distributed in Vietnam, Thailand, Malaysia, Indonesia, as well as South China.[52,53] Boat-fruited sterculia seed is commonly used in traditional Chinese medicine as a "coolant" for gastrointestinal disorders and soothing the throat.[52,54] Generally, boat-fruited sterculia seed is added into a large cup of boiling water and the liquid is consumed, then the absorbent seed is abandoned. One interesting phenomenon is that the absorbed water can expand boat-fruited sterculia seed significantly (Fig. 1). Although it has been used for hundreds of years in traditional Chinese medicinal prescriptions, its potential applications in material science have been ignored. In addition, detail investigations showed that boat-fruited sterculia seed is mainly consisted of polysaccharide.[52–54] Based on its volumetric swelling characteristics and chemical composition, we believe that the boat-fruited sterculia seed can act as a new source of carbonaceous materials for supercapacitor electrodes.

Herein, N-doped hierarchical porous carbon (NHPC) from waste boat-fruited sterculia was prepared by combining hydrothermal carbonization with KOH activation. The obtained NHPC showed a novel 3D interpenetrating macroporous network with micro- and mesopores. By the optimization of pore structure, the surface area and the doping of N atom, the waster boat-fruited sterculia derived NHPC exhibited high electrochemical capacitance, superior rate capability, extraordinary cycling stability as supercapacitor electrode materials.

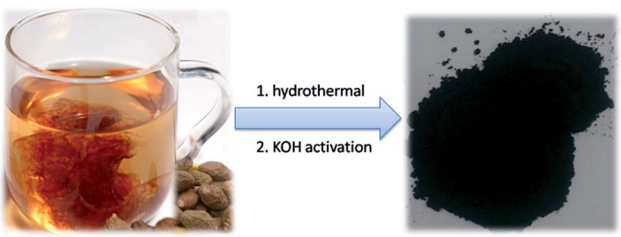

Fig. 1 Preparation process of the NHPC.

Experimental

Preparation of NHPC

500 mg of waste boat-fruited sterculia powder after removing peel and other nuggets, 500 mg of urea and 80 mL of deionized water were transferred into a 100 mL Teflon-lined stainless autoclave, successively. The autoclave was sealed and held at 180 °C for 12 h in oven for hydrothermal reaction, and then cooled to room temperature naturally. The obtained black precipitate was filtered and washed by water, and then dried at 80 °C for 12 h. Subsequently, the obtained precursor was immersed in potassium hydroxide solution with different mass ratio (KOH/precursor, 0.5–2) for 12 h and were dried at 80 °C and then was activated at a certain temperature (700–1000 °C) with a heating rate 5 °C min^{-1} under the inert gas of N_2. Finally, the as-obtained NHPC was soaked in 1 M HCl to remove any inorganic impurities and washed by distilled water until pH close to neutral, and then dried at 80 °C in oven. To distinguish the NHPC samples, the activated temperature and KOH/precursor ratio were marked on the name of samples, for example the NHPC-700-1 was prepared at activated temperature of 700 °C and KOH/precursor of 1.

Characterization

The morphology and microstructure of products were analyzed by scanning electron microscopy (SEM) (FEI, Quanta 450) and transmission electron microscopy (TEM) (JEOL, JEM 2100). The phase of the products was characterized using D8 Advance X-ray diffractometer (XRD) with Cu Kα radiation (λ = 1.5406 Å) operating at 40 mA and 40 kV. Raman spectra were recorded on a Lab RAM HR800 Laser Raman spectroscopy (HORIBA Jobin Yvon CO. Ltd) using a 647 nm argon ion laser. Nitrogen adsorption/desorption isotherms at 77 K using TriStar II 3020 surface area & pore size analyzer (Micromeritics) were employed to analyze specific surface area and pore size distribution based on BET (Brunauer–Emmett–Teller) and nonlocal density functional theory (NLDFT), respectively. X-ray photoelectron spectroscopy (XPS) was conducted with an Axis Ultra (Kratos) XPS spectrometer.

Electrochemical measurements

All the electrochemical measurements were tested by Chenhua's CHI660C electrochemical working station (Shanghai, China) in 6 M KOH at room temperature (~20 °C). The electrochemical properties of the NHPC electrodes were investigated under a three-electrode cell configuration with platinum foil as counter electrode and Hg/HgO electrode as reference electrode. The working electrodes were fabricated by mixing 90 wt% active materials, 10 wt% polyvinylidene fluoride (PVDF) (as the binder) dissolved in *N*-methyl-2-pyrrolidone to form a slurry, and the slurry was coated onto a nickel foam as current collector. The amount and effective area of active materials on each current collector was about 2–3 mg cm^{-2}, respectively. The as-prepared working electrodes were dried at 80 °C in oven overnight. Furthermore, to evaluate the capacitive performance of the NHPC electrodes in a full-cell configuration, NHPC-based

symmetric supercapacitor devices were fabricated as follows: the prepared NHPC electrodes were used as positive electrode and negative electrode, respectively, and pressed together and separated by a polypropylene membrane separator. Cyclic voltammetry (CV) curves were obtained under different scan rates from 10 to 200 mV s^{-1}. Galvanostatic charge/discharge (GCD) measurement was performed under different current densities from 1 to 50 A g^{-1}. The electrochemical impedance spectroscopy (EIS) was obtained in the frequency range from 100 kHz to 0.01 Hz with an amplitude of 5 mV.

The gravimetric specific capacitances of NHPC electrodes in three-electrode system and NHPC-based symmetric supercapacitors were calculated from the GCD curves using the following eqn (1) and eqn (2), respectively:

$$C = \frac{I \times \Delta t}{m \times \Delta V} \quad (1)$$

$$C = \frac{2I \times \Delta t}{m \times \Delta V} \quad (2)$$

where C (F g^{-1}) represents the specific capacitance of the active material, I (A) refers to the discharge current, ΔV (V) corresponds to the potential change within the discharge time Δt (s). In three-electrode system, m (g) represents the mass loading of active material in a single electrode, in two-electrodes cell, m (g) is the mass loading of active materials based on both electrodes.

The energy density (E, W h kg^{-1}) and power density (P, W kg^{-1}) were calculated from the following eqn (3) and (4):

$$E = \frac{1}{2} C(\Delta V)^{\frac{1}{2}} \quad (3)$$

$$P = \frac{E}{\Delta t} \quad (4)$$

Results and discussion

Morphology and structure

The fabrication process of the NHPC is shown in Fig. 1. First, waste boat-fruited sterculia seed was carbonized by hydrothermal reaction in an autoclave with the aid of urea, and then, the obtained power was further activated by KOH. Fig. 2a and b shows the typical SEM images of the as-prepared NHPC derived from waste boat-fruited sterculia seed. It can be observed that the obtained NHPC exhibits a 3D structure, and some macropores up to several microns can be seem on the surface of the NHPC. The typical TEM image (Fig. 2c) of NHPC sample exhibits that these macropores penetrate the entire carbon material and are interpenetrating each other. The novel structure with interpenetrating macropores can effectively improve the contact between the electrode materials and the electrolyte, and shorten the pathways of ions diffusion and offer minimized diffusive resistance to mass transport on the interface between electrode and electrolyte.[36,40,48,55] We cannot observe evident lattice fringe in the typical HTEM image of NHPC (Fig. 2d), and the selected-area electron diffraction (SAED) pattern (inset in Fig. 2d) suggests that the NHPC is amorphous structure.

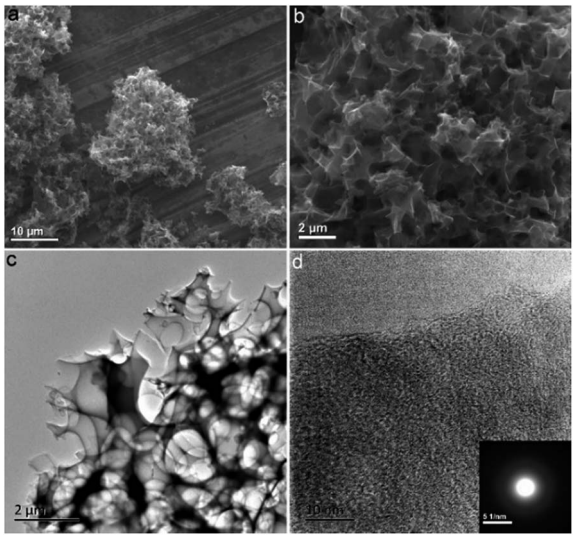

Fig. 2 Typical (a and b) SEM, (c) TEM and (d) HRTEM images of NPHC.

X-ray diffraction (XRD) was used to characterize the microstructure of the NHPC samples. Fig. 3a shows the XRD patterns of NHPC, and we can observe only two bread-like pattern of

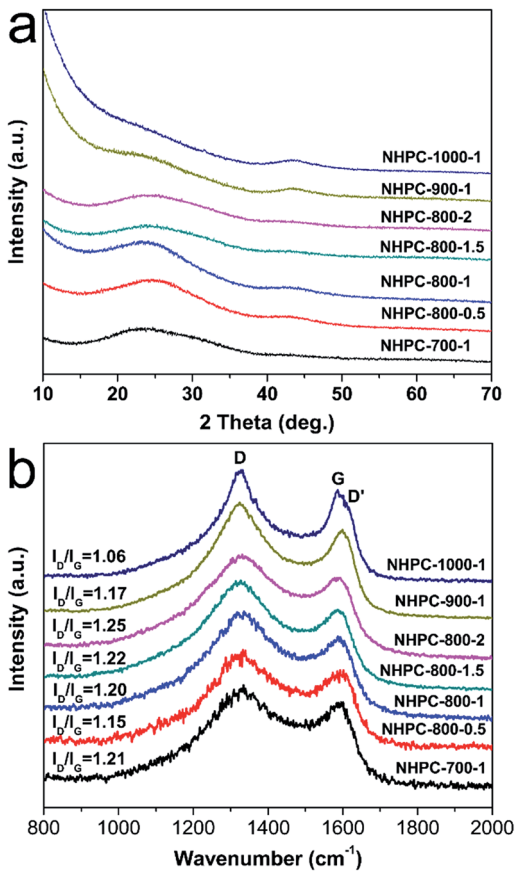

Fig. 3 (a) XRD patterns and (b) Raman spectra of NHPC samples.

diffuse scattering peaks at about $2\theta = 26$ and 44°, but not with the crystalline material corresponding to the sharp diffraction peaks, indicating NHPC samples having an amorphous structure. In addition, the intensity of peak at 44° is gradually weakened with the ratio of KOH/precursor from 0.5 to 2 under the activation temperature of 800 °C, but increased when the activation temperature increased from 700 to 1000 °C. It indicates that the increased ratio of KOH/precursor can evidently increase the amorphous of NHPC. On the contrary, the high activation temperature can effectively improve the graphitization of NHPC. Moreover, the high diffraction intensity in the low angle of diffraction region suggests these NHPC samples have abundant pores. The microstructure of NHPC was further analysed by the Raman spectroscopy, and the corresponding Raman spectra of NHPC samples were presented in Fig. 3b. The Raman spectra of NHPC samples can be fitted to two characterization peaks at around 1335 cm^{-1} (D band) and 1585 cm^{-1} (G band) by Lorentzian. The D band is ascribed to A_{1g} mode which is attributed to the crystal defects and disordered structures in carbon materials, while the G band corresponds to the first-order scattering of the E_{2g} mode observed for sp^2-C domains.[43,56] Generally, the intensity ratio of D band to G band (I_D/I_G) is used to evaluate the graphitization degree of carbon materials. Based on the results fitted by Lorentzian, the intensity ratio of I_D/I_G for NHPC-700-1, NHPC-800-0.5, NHPC-800-1, NHPC-800-1.5, NHPC-800-2, NHPC-900-1 and NHPC-1000-1 is 1.21, 1.15, 1.20, 1.22, 1.25, 1.17 and 1.06, respectively. It indicates that the graphitization of NHPC was enhanced with the increase of activation temperature, but the crystal defects and disordered structures in the NHPC were increased with the increase of activated agent of KOH. In addition, a slight shoulder at 1615 cm^{-1} in the Raman spectrum of NHPC-1000-1 is ascribed to the D′ band, which corresponds to a defect structure of graphite[57] even if the activation temperature was up to 1000 °C.

For the electrode materials of EDLCs, the specific surface area and pore structure of materials are two key factors in improving the energy storage capacity.[4,58] Therefore, the nitrogen adsorption–desorption experiment of NHPC samples were carried out at 77 K, and the obtained results are shown in Fig. 4. The adsorption–desorption isotherms of NHPC-700-1, NHPC-800-0.5, NHPC-800-1, NHPC-800-1.5 and NHPC-800-2 samples (Fig. 4a) are identified as type I with a sharp adsorption in the area of low relative pressure ($P/P_0 < 0.1$), adsorption plateaus appear at the area of moderate relative pressure ($0.1 < P/P_0 < 0.45$) and moderate H4 hysteresis loops at the area of high relative pressure ($P/P_0 > 0.45$), indicating significant microporous structure with a limited number of mesopores. The

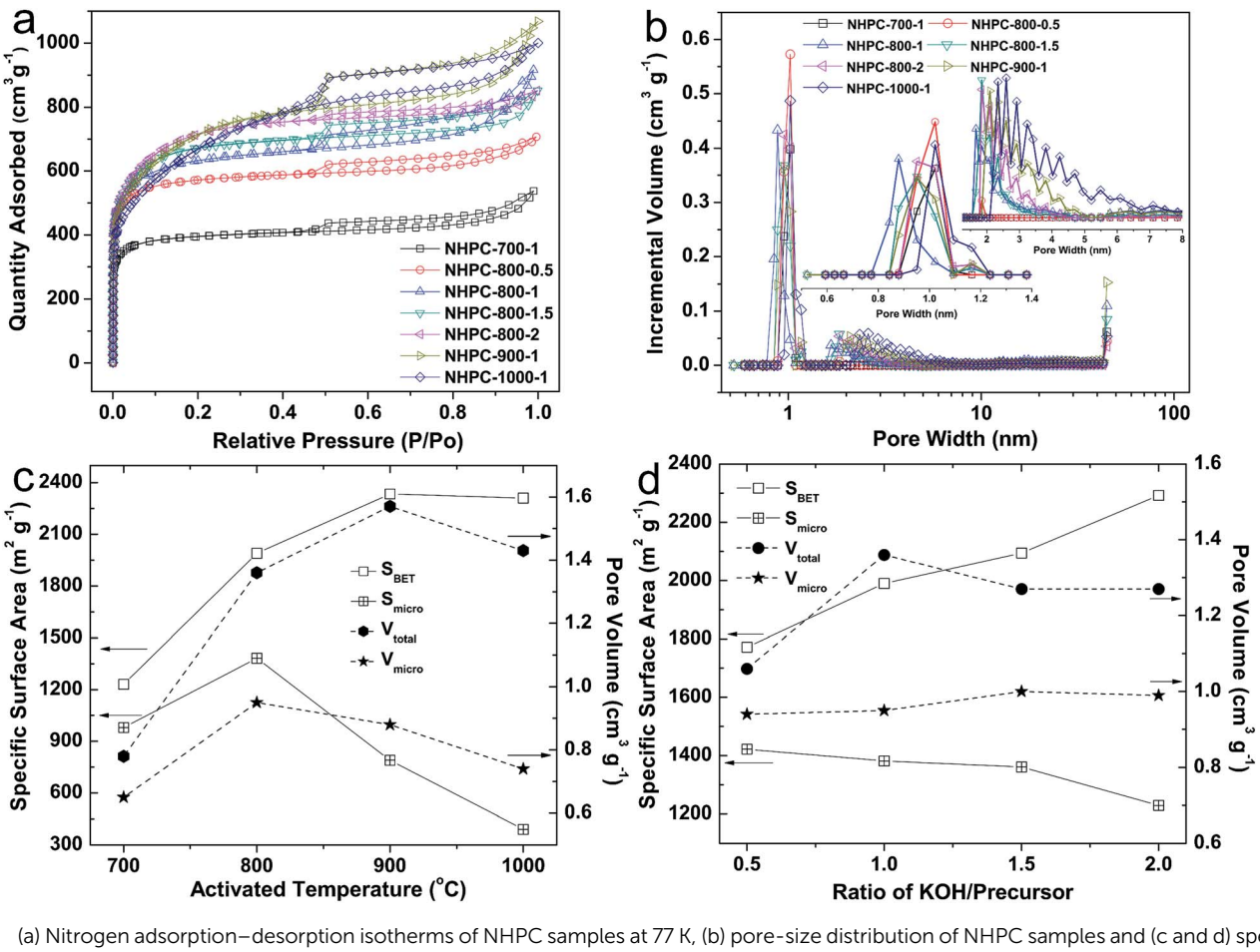

Fig. 4 (a) Nitrogen adsorption–desorption isotherms of NHPC samples at 77 K, (b) pore-size distribution of NHPC samples and (c and d) specific surface area and pore volume of NHPC samples prepared at different activation temperature and different KOH/precursor ratios.

adsorption–desorption isotherm of NHPC-900-1 and NHPC-1000-1 shows a combination of type I and type IV with an intense adsorption at the area of low relative pressure and a type H4 hysteresis loop in the medium P/P_0 range, indicating the samples possess micropores and mesopores. Moreover, all isotherms exhibit a sharp increase of N_2 capture at high pressure near 1.0 of P/P_0, which manifests the presence of macropores. Fig. 4b shows the pore distribution of all NHPC samples from the NLDF model, it indicates that all NHPC samples have micropore, mesopore and macropores. From Fig. 4b, the porosity of the NHPC-700-1 and NHPC-800-0.5 is made up mostly of micropores with a strong peak at 1.02 nm for the low activation condition. As the KOH/precursor ratio increases, for the activated samples of NHPC-800-1, NHPC-800-1.5 and NHPC-800-2, the strong micropore peak is 0.88, 0.95 and 0.95 nm, respectively. In addition, other two peaks at around 1.16 and 1.7 nm appear in the above three NHPC samples. When the activation temperature increases to 1000 °C, the strong micropore peak expands to 1.02 nm. Compared with other NHPC samples, the micropore distribution of NHPC-800-1 is more narrow, which is beneficial to the energy storage capacity of the EDLCs materials.[59–61] As shown in Fig. 4b, we can observe that the mesopores in NHPC-700-1 and NHPC-800-0.5 samples is rare. As the activation temperature or KOH/precursor ratio increases, the content of mesopores in NHPC samples increases gradually, and we can see that NHPC-900-1 and NHPC-1000-1 samples contain a large fraction of mesopores with a size of around 2.5 nm. Actually, the mesopore structures are of great importance for energy storage because of the reduced porous tortuosity and facilitated ion transport.[55,62] Meanwhile, the macropores are favorable for buffering ions to shorten the diffusion distances from the external electrolyte to the interior surfaces.[55]

For better understanding, the textural parameters are compared in Fig. 4c and d. Fig. 4c shows that the specific surface area and pore volume of NHPC samples prepared at different activation temperature. With the increase of activation temperature, the specific surface area (S_{BET}) obviously rises from 1231 at 700 °C to 2334 $m^2\ g^{-1}$ at 900 °C, and remains 2310 $m^2\ g^{-1}$ at 1000 °C. Similarly, the total pore volume (V_{total}) of NHPC increases from 0.78 $cm^3\ g^{-1}$ at 700 °C to 1.57 $cm^3\ g^{-1}$ at 900 °C, and remains 1.43 $cm^3\ g^{-1}$ at 1000 °C. In addition, the change of *t*-plot micropore area (S_{micro}) of NHPC exhibits peak-like shape with the rapidly increasing from 980 $m^2\ g^{-1}$ at 700 °C to 1380 $m^2\ g^{-1}$ at 800 °C and then suddenly decreasing to only 390 $m^2\ g^{-1}$ at 1000 °C. Meanwhile, the micropore volume (V_{micro}) of NHPC is up to 0.95 $cm^3\ g^{-1}$ at 800 °C, and then gradually reduces to 0.74 $cm^3\ g^{-1}$ at 1000 °C. The above results indicate that part of micropores were transformed to mesopores or macropores at the higher activation temperature of 900 and 1000 °C. As we known, the micropores are the main contributors for the capacitance of EDLCs of activated carbon.[27,63–65] Therefore, the 800 °C is the suitable temperature for the activation of carbon form waste boat-fruited sterculia seed. Fig. 4d shows the specific surface area and pore volume of NHPC samples prepared at different KOH/precursor ratios. S_{BET} of NHPC gradually increases from 1772 to 2292 $m^2\ g^{-1}$ with the increase of KOH/precursor ratio from 0.5 to 2. However, the V_{total} of NHPC raises from 1.06 to 1.36 $cm^3\ g^{-1}$ with the increase of KOH/precursor ratio from 0.5 to 1, and then drops and remains 1.27 $cm^3\ g^{-1}$ at the KOH/precursor ratio of 1.5 and 2. The S_{micro} of NHPC slowly decreases with the increase of the KOH/precursor ratio from 0.5 to 2, and the corresponding S_{micro} at different KOH/precursor ratio is 1422, 1382, 1361 and 1229 $m^2\ g^{-1}$ for the KOH/precursor ratio of 0.5, 1, 1.5, 2, respectively. The V_{micro} at different KOH/precursor ratio is relatively stable, and the V_{micro} of the KOH/precursor ratio of 0.5, 1, 1.5, 2 is 0.94, 0.95, 1.00 and 0.99 $cm^3\ g^{-1}$, respectively.

The doping of heteroatom such as O, N in the surface can also further improve the energy storage of activated materials.[29,66–68] Therefore, the element and corresponding chemical states in the surface of NHPC samples were determined by XPS. Fig. 5 shows the XPS results of carbon from waste boat fruited sterculia seed at different activation temperature and KOH/precursor ratios. Fig. 5a shows C, O and N elements in the prepared NHPC samples. The detail change of O and N element in NHPC are presented in Fig. 5b and c. When the ratio of KOH/precursor is 1, both O and N atoms in NHPC decrease with increasing activation temperature. The contents of O and N element drop from 6.46 and 5.45 atom% for NHPC-700-1 activated at 700 °C to 1.76 and 0.92 atom% for NHPC-1000-1 activated at 1000 °C, respectively. In addition, as the mass ratio of KOH/precursor continually increases, while the nitrogen content is a gradual decrease, from 2.81 atom % for NHPC-800-0.5 activated at KOH/precursor of 0.5 to 2.42 atom% for NHPC-800-1 activated at KOH/precursor of 1, and 1.68 atom% for NHPC-800-2 obtained at KOH/precursor of 2. This phenomenon is consistent with the previous reports about activated nitrogen-containing carbons.[69,70] It suggests that nitrogen is oxidized and more easily removed than carbon during the activation process. However, the content of O in NHPC is gradually up to 9.22 atom% for NHPC-800-2 from 5.53 atom% for NHPC-0.5 with the increasing KOH/precursor ratio. Fig. 5d and S1† shows the high-resolution spectra of N 1s, all N 1s spectra of NHPC can be deconvoluted into four peaks at around 398.3, 399.6, 400.6 and 402.7 eV, which are corresponding to the pyridinic-N (N-6), pyrrolic-N (N-5), quaternary-N (N-Q) and pyridinic N–oxide groups (N–O), respectively. Moreover, the relative atomic ratios and the changing of each type of N species in NHPC samples are summarized in Fig. 5e and S2† which show that the proportion of N-6 and N-Q increases, but N-5 and N–O decreases, as the activation temperature increases, indicating that N-6 and N-Q are more stable than N-5 and N–O at higher activation temperature (Fig. S2a†). However, with the increase of KOH/precursor ratio (Fig. S2b†), the content of N-6 and N-Q decreases, but N-5 and N–O increase, suggesting that parts of N-6 and N-Q may transfer to N-5 and N–O at high KOH/precursor ratio.

Electrochemical performance of NHPC materials for supercapacitors

Cyclic voltammetry (CV) and galvanostatic charge/discharge (GCD) was used to characterize the capacitive properties of the prepared NHPC samples in 6 M KOH solution in three-electrode system. Fig. 6a and b shows CV curves of all NHPC

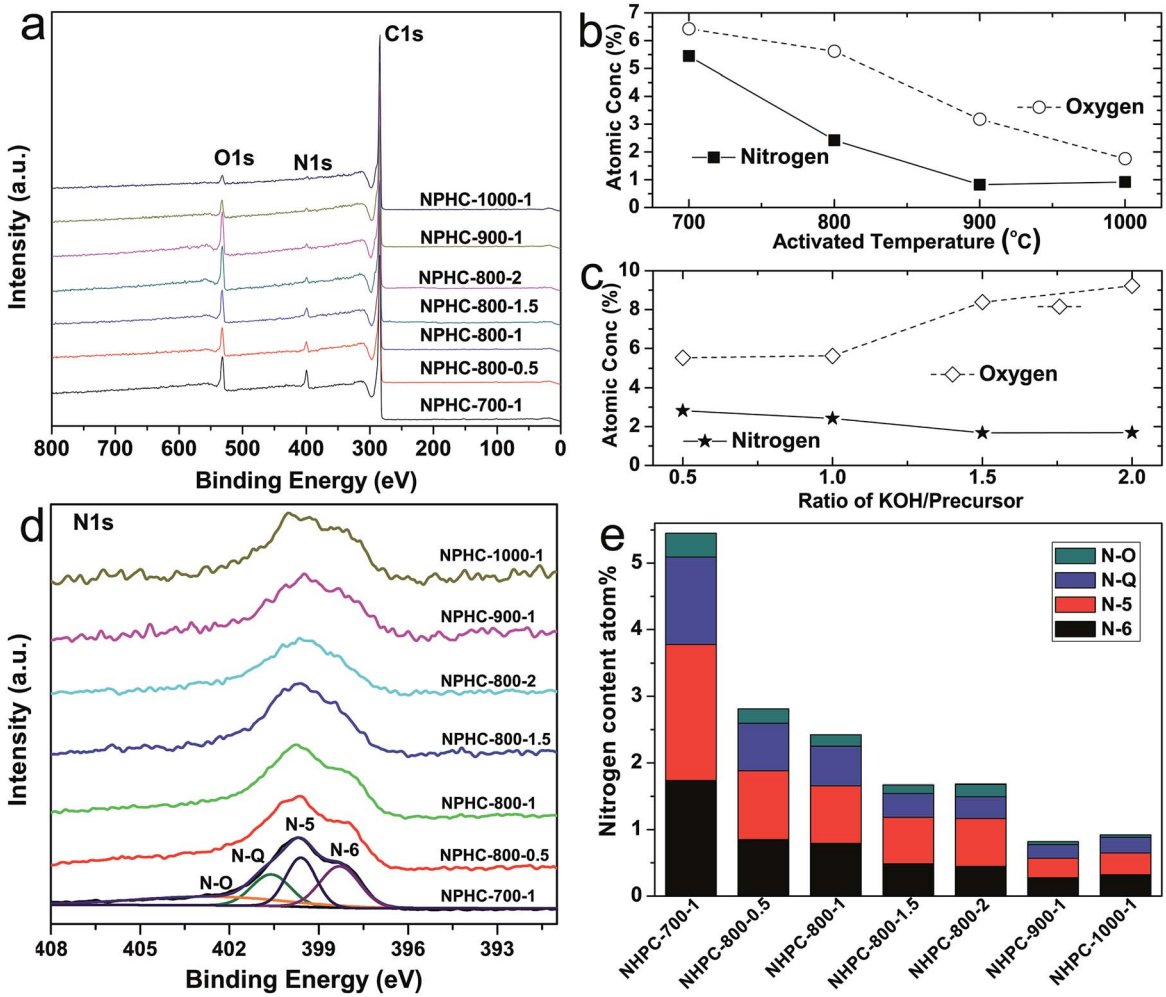

Fig. 5 XPS results of boat-fruited-sterculia-derived carbon (a) spectrum of C 1s (b), N 1s (c) and O 1s (d), and (e) the detail of different N including pyridinic-N (N-6), pyrrolic-N (N-5), quaternary-N (N-Q) and pyridinic N–oxide groups (N–O).

samples at 10 mV s^{-1}. All of CV curves present rectangular-like shape, implying mainly electrical double-layer capacitive behavior. A negligible broad peak about at 0.8 V can be attributed to the super imposition of several redox reactions that may be the contribution of nitrogen and oxygen functionalities,[36,71–73] which can effectively increase the capacitance of electron storage. Fig. 6a shows that the capacitance of the NHPC samples at different activation temperature based on the area of CV curves in alkaline electrolytes decreases in the following order: NHPC-800-1 > NHPC-900-1 > NHPC-1000-1 > NHPC-700-1. In addition, Fig. S3a† illustrates the GCD curves of NHPC at different activated temperature, and the order of capacitances calculated from the discharge curves is consistent with the CV results. Therefore, optimal activation temperature is 800 °C. From N_2 sorption isotherms (Fig. 4a), the surface area and pore volume of the NHPC-700-1 are the lowest in all carbon samples. However, the capacitance of NHPC materials is not directly dependent on the specific surface areas and pore volume. NHPC-800-1 shows the best performance in 6 M KOH because it possesses high micropore surface area (1382 m^2 g^{-1}), large pore volume (V_{total} = 1.36 cm^3 g^{-1}, V_{micro} = 0.95 cm^3 g^{-1}) and a moderate N-doping level (2.48% obtained by XPS). The optimized pore structure and the doping of heteroatoms can effectively increase the capacitance of NHPC materials. Fig. 6b and S3b† shows the CV and GCD curves of NHPC samples under different KOH/precursor ratios, respectively, it indicates that the capacitance of NHPC-800-1 is obviously larger than NHPC-800-0.5, NHPC-800-1.5 and NHPC-800-2. It can be attributed to the NHPC-800-1 has the high micropore surface area (1382 m^2 g^{-1}), rational micro/mesopore ratio and a moderate N-doping level. Furthermore, the narrow micropore size distribution of NHPC-800-1 may play important role for the high capacitance.

Therefore, the electrochemical properties of NHPC-800-1 were analyzed in detail, and CV curves are shown in Fig. 6c. It is observed that the CV area increases with the increasing sweep rates. In addition, GCD tests were used to further evaluate the capacitive properties of the prepared NHPC-800-1, and the corresponding curves and the calculated capacitances were presented in Fig. 6d and e. All GCD curves of NHPC-800-1 show only very small *IR* drops of 4.1, 7.5 and 19 mV at current densities of 1, 2 and 5 A g^{-1}, respectively. The gravimetric

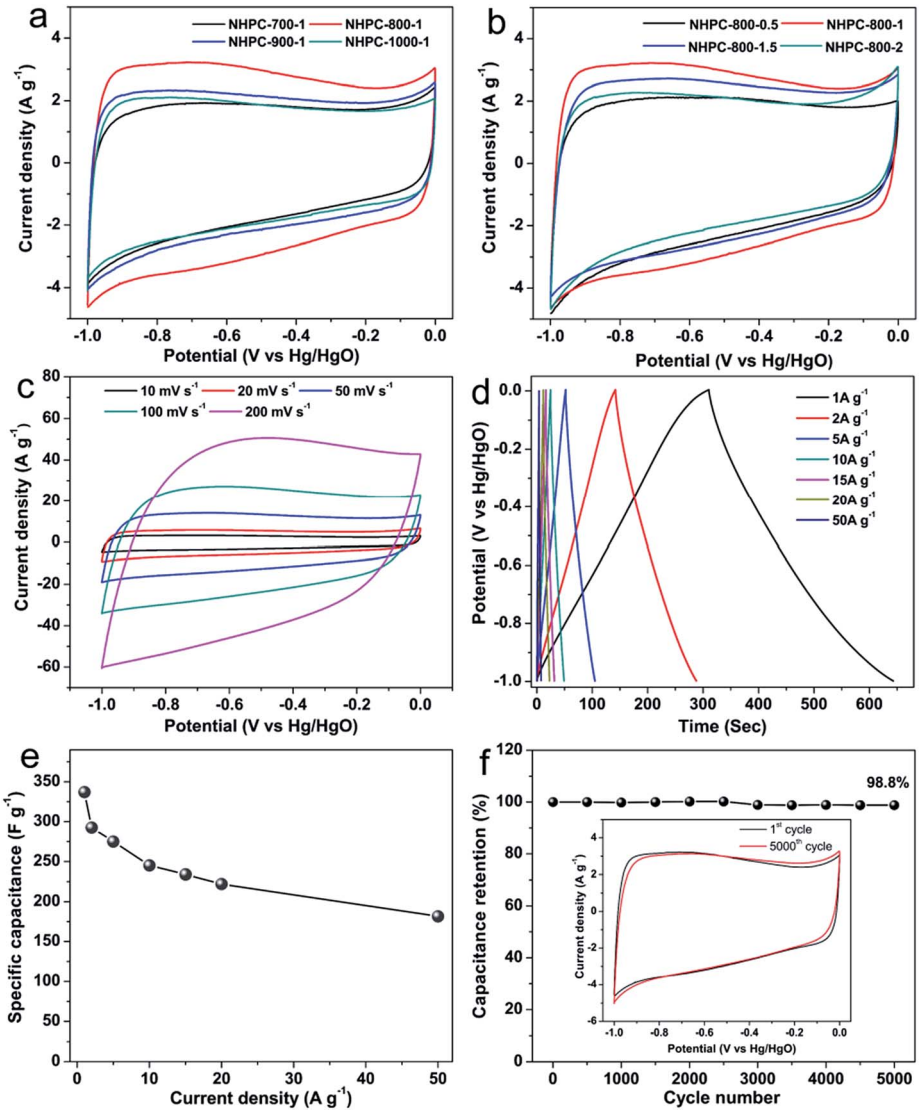

Fig. 6 (a) CV curves of NHPC-700-1, NHPC-800-1, NHPC-900-1 and NHPC-1000-1 at a scan rate of 10 mV s^{-1}; (b) CV curves of NHPC-800-0.5, NHPC-800-1, NHPC-800-1.5 and NHPC-800-2 at 10 mV s^{-1}; (c) CV curves of NHPC-800-1 at different scan rates; (d) charge/discharge curves of NHPC-800-1 at various current densities; (e) specific capacitance of NHPC-800-1 as a function of current density; (f) cycling stability of NHPC-800-1 at 20 A g^{-1} up to 5000 cycle.

specific capacitance of NHPC-800-1 calculated from the GCD curves is 337 F g^{-1} at 1 A g^{-1}, and retains high values of 245 (72.7% capacitance retention), 234 (69.4% capacitance retention), 222 (65.9% capacitance retention) at 10, 15 and 20 A g^{-1}, respectively. Even the current densities of increases to 50 A g^{-1} (Fig. 6e), the NHPC-800-1 still delivers high specific capacitance up to 181.5 F g^{-1} of (53.7% capacitance retention). Compared with the other NHPC samples (Fig. S4†), it indicates that NHPC-800-1 exhibits superior rate capability. The cycle stability of NHPC-800-1 at high current density of 20 A g^{-1} is shown in Fig. 6f. After 5000 cycles, NHPC-800-1 remains 98.8% of initial specific capacitance, and the CV curves of the NHPC-800-1 electrode before and after the long-term cycling test measured at 10 mV s^{-1} shown in inset of Fig. 6f exhibit similar profiles without clear changes, indicating superior cycling stability of NHPC-800-1. Moreover, the superior stability of the NHPC-800-1 was confirmed by the Nyquist plots before and after 10 000 GCD cycles in Fig. S5.† Both before and after 10 000 GCD, the high-frequency semicircle shows that the charge-transfer resistance of the NHPC-800-1 is low, and the slight increase after 10 000 cycles can probably be ascribed to oxidation of the carbon electrode caused by oxygen dissolved in the electrolytes.[36] The short Warburg region at the slope of 45° portion of the curve suggests good ion diffusion in the NHPC-800-1 electrode.[4] The low-frequency region is almost vertical, indicating that the NHPC-800-1 electrode has a nearly ideal capacitive behavior.[24]

Electrochemical performance of NHPC-800-1 fabricated symmetric supercapacitor

To further investigate the excellent supercapacitor performances of NHPC-800-1, a symmetric supercapacitor fabricated

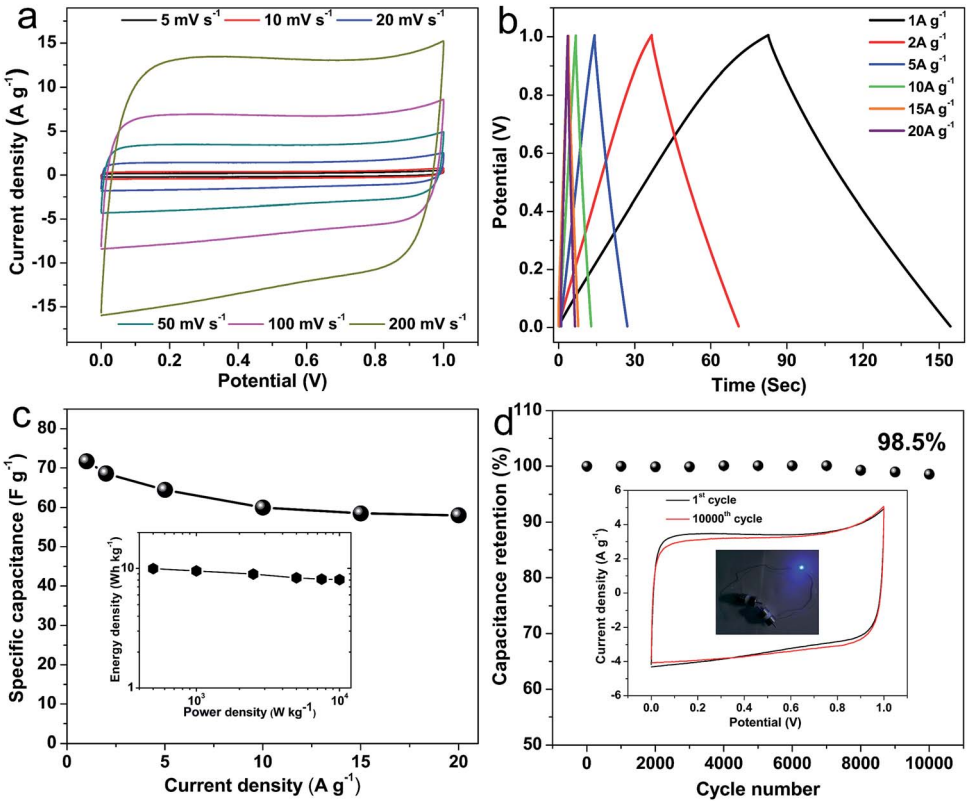

Fig. 7 Electrochemical performances of a symmetrical supercapacitor prepared by NHPC-800-1 in 6 M KOH electrolyte. (a) CV curves at various scan rates, (b) GCD curves for various current densities, (c) the functional relation between specific capacitance and current density, (d) cycling stability at 20 A g^{-1} for up to 10 000 cycles.

by NHPC-800-1 was evaluated in 6 M KOH. Fig. 7a shows the CV curves of the symmetric supercapacitor based on NHPC-800-1, which possess rectangular shapes in the voltage windows ranging from 0–1.0 V, even at a high scan rate of 200 mV s^{-1}. It indicates good EDLC behavior and high rate performance. Fig. 7b shows the GCD curves of the NHPC-800-1 based symmetric supercapacitor at different current densities. The nearly symmetric GCD curves with a slight *IR* drop further reveal good capacitive characteristics for the symmetrical supercapacitor. Fig. 7c shows the specific capacitances calculated based the GCD curves of Fig. 7b at various current densities. The specific capacitance is 72.3 F g^{-1} at 0.5 A g^{-1}, 64.5 F g^{-1} at 5 A g^{-1} and 60 F g^{-1} at 10 A g^{-1}, respectively. It remains 58 F g^{-1} with a capacitance retention up to 80.2% at 20 A g^{-1}, which exhibits superior rate capability. Furthermore, the Ragone plot (inset of Fig. 7c) indicates that the NHP-800-1 based symmetric supercapacitor possesses an energy density of 10.04 W h kg^{-1} with a power density of 250 W kg^{-1} at a current density of 0.5 A g^{-1}. When the current increases to 20 A g^{-1}, the energy density of 8.05 W h kg^{-1} can be still retained at a power density of 10 kW kg^{-1}, which is better than most of porous carbon materials in alkaline electrolyte.[74] The long cycle life of the NHPC-800-1-based symmetric supercapacitor was evaluated by repeating the GCD test at 20 A g^{-1}, and the capacitance retention is up to 98.5% after 10 000 cycles (Fig. 7d), which means that the structure and performance of NHPC-800-1 are not change during the process of long-term cycling tests and highlights the super electrochemical stability and outstanding reversibility of the symmetric supercapacitor. It is not obvious change that the profile of carve after the long-term cycling compared with before the cycle. Finally, a tandem device composed of connecting two prototype units (inset of Fig. 7d) can be used to light up a blue light emitting diode, further demonstrating that NHPC-800-1 materials have great potential application for supercapacitor.

Conclusions

A series of N-doped hierarchical porous carbons were prepared from waste boat-fruited sterculia seed by hydrothermal carbonization and KOH activation. The resulting activated carbons have large specific area and pore volume, hierarchical porous structure including micropore, mesopore and macropore, and robust surface chemistries. Among of these carbons, the NHPC-800-1 electrode can deliver high specific capacitances up to 337 F g^{-1} at a current density of 1 A g^{-1}, even 181.5 F g^{-1} at a current density of 50 A g^{-1} in 6 M KOH. The NHPC-800-1 fabricated symmetrical supercapacitor can deliver a specific energy density of 8.05 W h kg^{-1} and a specific power density of 10 kW kg^{-1} and a stable cycle life over 10 000 cycles at a current density of 20 A g^{-1}. The materials, which are synthesized from waste boat-fruited sterculia seed, offer a promising approach

for the development of novel capacitive-based energy storage systems.

Acknowledgements

This work was supported by the National Natural Science Foundation of China (51402146), the National Science Funds for Excellent Young Scholars (51422807), the Science and Technology Planning Project (20151BBG70019) of Jiangxi province. Prof. L. Guo appreciated the GanPo 555 Talent Project of Jiangxi Province.

Notes and references

1 P. Simon and Y. Gogotsi, *Nat. Mater.*, 2008, **7**, 845–854.
2 J. R. Miller and P. Simon, *Science*, 2008, **321**, 651–652.
3 E. Frackowiak, *Phys. Chem. Chem. Phys.*, 2007, **9**, 1774–1785.
4 L. L. Zhang and X. S. Zhao, *Chem. Soc. Rev.*, 2009, **38**, 2520.
5 Y. Zhai, Y. Dou, D. Zhao, P. F. Fulvio, R. T. Mayes and S. Dai, *Adv. Mater.*, 2011, **23**, 4828–4850.
6 A. Jänes, H. Kurig and E. Lust, *Carbon*, 2007, **45**, 1226–1233.
7 T. H. L. D. T. Pham, D. H. Luong, F. Yao, A. Ghosh, V. T. Le, T. H. Kim, B. Li, J. Chang and Y. H. Lee, *ACS Nano*, 2015, **9**, 2018–2027.
8 L. Jiang and Z. Fan, *Nanoscale*, 2014, **6**, 1922–1945.
9 Z. Bo, W. Zhu, W. Ma, Z. Wen, X. Shuai, J. Chen, J. Yan, Z. Wang, K. Cen and X. Feng, *Adv. Mater.*, 2013, **25**, 5799–5806.
10 A. Alabadi, S. Razzaque, Y. Yang, S. Chen and B. Tan, *Chem. Eng. J.*, 2015, **281**, 606–612.
11 W. Chaikittisilp, M. Hu, H. Wang, H.-S. Huang, T. Fujita, K. C. W. Wu, L.-C. Chen, Y. Yamauchi and K. Ariga, *Chem. Commun.*, 2012, **48**, 7259–7261.
12 H. Liu, P. He, Z. Li, Y. Liu and J. Li, *Electrochim. Acta*, 2006, **51**, 1925–1931.
13 Y. Z. Zhang, T. Cheng, Y. Wang, W. Y. Lai, H. Pang and W. Huang, *Adv. Mater.*, 2016, **28**, 5242–5248.
14 H. Wan, J. Jiang, Y. Ruan, J. Yu, L. Zhang, H. Chen, L. Miao and S. Bie, *Part. Part. Syst. Charact.*, 2014, **31**, 857–862.
15 P. Zhang, J. Zhou, W. Chen, Y. Zhao, X. Mu, Z. Zhang, X. Pan and E. Xie, *Chem. Eng. J.*, 2017, **307**, 687–695.
16 S. Zhang, B. Yin, Z. Wang and F. Peter, *Chem. Eng. J.*, 2016, **306**, 193–203.
17 B. P. Bastakoti, H. Oveisi, C.-C. Hu, K. C. W. Wu, N. Suzuki, K. Takai, Y. Kamachi, M. Imura and Y. Yamauchi, *Eur. J. Inorg. Chem.*, 2013, **2013**, 1109–1112.
18 H. S. Huang, K. H. Chang, N. Suzuki, Y. Yamauchi, C. C. Hu and K. C. Wu, *Small*, 2013, **9**, 2520–2526.
19 B. P. Bastakoti, Y. Kamachi, H.-S. Huang, L.-C. Chen, K. C. W. Wu and Y. Yamauchi, *Eur. J. Inorg. Chem.*, 2013, **2013**, 39–43.
20 Z. Wang, D. O. Carlsson, P. Tammela, K. Hua, P. Zhang, L. Nyholm and M. Stromme, *ACS Nano*, 2015, **9**, 7563–7571.
21 D. P. Dubal, S. H. Lee, J. G. Kim, W. B. Kim and C. D. Lokhande, *J. Mater. Chem.*, 2012, **22**, 3044.
22 C. Yang, L. Zhang, N. Hu, Z. Yang, Y. Su, S. Xu, M. Li, L. Yao, M. Hong and Y. Zhang, *Chem. Eng. J.*, 2017, **309**, 89–97.
23 R. R. Salunkhe, S. H. Hsu, K. C. Wu and Y. Yamauchi, *ChemSusChem*, 2014, **7**, 1551–1556.
24 Y. Zhu, S. Murali, M. D. Stoller, K. J. Ganesh, W. Cai, P. J. Ferreira, A. Pirkle, R. M. Wallace, K. A. Cychosz, M. Thommes, D. Su, E. A. Stach and R. S. Ruoff, *Science*, 2011, **332**, 1537–1541.
25 T. Chen and L. Dai, *Mater. Today*, 2013, **16**, 272–280.
26 X. Li and B. Wei, *Nano Energy*, 2013, **2**, 159–173.
27 E. Redondo, J. Carretero-González, E. Goikolea, J. Ségalini and R. Mysyk, *Electrochim. Acta*, 2015, **160**, 178–184.
28 G. Chen, S. Wu, L. Hui, Y. Zhao, J. Ye, Z. Tan, W. Zeng, Z. Tao, L. Yang and Y. Zhu, *Sci. Rep.*, 2016, **6**, 19028.
29 L.-F. Chen, X.-D. Zhang, H.-W. Liang, M. Kong, Q.-F. Guan, P. Chen, Z.-Y. Wu and S.-H. Yu, *ACS Nano*, 2012, **6**, 7092–7102.
30 D. N. Futaba, K. Hata, T. Yamada, T. Hiraoka, Y. Hayamizu, Y. Kakudate, O. Tanaike, H. Hatori, M. Yumura and S. Iijima, *Nat. Mater.*, 2006, **5**, 987–994.
31 Q. Wang, Z. H. Wen and J. H. Li, *Adv. Funct. Mater.*, 2006, **16**, 2141–2146.
32 C. Liu, Z. Yu, D. Neff, A. Zhamu and B. Z. Jang, *Nano Lett.*, 2010, **10**, 4863–4868.
33 Y. Zhao, M. Liu, X. Deng, L. Miao, P. K. Tripathi, X. Ma, D. Zhu, Z. Xu, Z. Hao and L. Gan, *Electrochim. Acta*, 2015, **153**, 448–455.
34 P. Zhang, Z.-A. Qiao, Z. Zhang, S. Wan and S. Dai, *J. Mater. Chem. A*, 2014, **2**, 12262–12269.
35 Y. Lv, L. Gan, M. Liu, W. Xiong, Z. Xu, D. Zhu and D. S. Wright, *J. Power Sources*, 2012, **209**, 152–157.
36 Y. Dong, W. Wang, H. Quan, Z. Huang, D. Chen and L. Guo, *ChemElectroChem*, 2016, **3**, 814–821.
37 S. Song, F. Ma, G. Wu, D. Ma, W. Geng and J. Wan, *J. Mater. Chem. A*, 2015, **3**, 18154–18162.
38 R. R. Salunkhe, J. Tang, Y. Kamachi, T. Nakato, J. H. Kim and Y. Yamauchi, *ACS Nano*, 2015, **9**, 6288–6296.
39 Z. Li, W. Lv, C. Zhang, B. Li, F. Kang and Q.-H. Yang, *Carbon*, 2015, **92**, 11–14.
40 X. Wu, L. Jiang, C. Long and Z. Fan, *Nano Energy*, 2015, **13**, 527–536.
41 J. Ma, Y.-z. Dong, L. Wang, P. Yu, H.-j. Yan, C.-g. Tian, J.-h. Li and H.-g. Fu, *ChemistrySelect*, 2016, **1**, 2167–2173.
42 H. Luo, Z. Liu, L. Chao, X. Wu, X. Lei, Z. Chang and X. Sun, *J. Mater. Chem. A*, 2015, **3**, 3667–3675.
43 J. Zhou, J. Lian, L. Hou, J. Zhang, H. Gou, M. Xia, Y. Zhao, T. A. Strobel, L. Tao and F. Gao, *Nat. Commun.*, 2015, **6**, 8503.
44 L.-Z. Fan, S. Qiao, W. Song, M. Wu, X. He and X. Qu, *Electrochim. Acta*, 2013, **105**, 299–304.
45 T. Lin, W. Chen, F. Liu, C. Yang, H. Bi, F. Xu and F. Huang, *Science*, 2015, **350**, 1508–1513.
46 J. Hou, C. Cao, F. Idrees and X. Ma, *ACS Nano*, 2015, **9**, 2556–2564.
47 G. A. Ferrero, A. B. Fuertes and M. Sevilla, *J. Mater. Chem. A*, 2015, **3**, 2914–2923.
48 Z. Li, L. Zhang, B. S. Amirkhiz, X. Tan, Z. Xu, H. Wang, B. C. Olsen, C. M. B. Holt and D. Mitlin, *Adv. Energy Mater.*, 2012, **2**, 431–437.
49 H. Chen, D. Liu, Z. Shen, B. Bao, S. Zhao and L. Wu, *Electrochim. Acta*, 2015, **180**, 241–251.

50 H. Sun, L. Cao and L. Lu, *Energy Environ. Sci.*, 2012, **5**, 6206–6213.
51 Y. Gao, W. Zhang, Q. Yue, B. Gao, Y. Sun, J. Kong and P. Zhao, *J. Power Sources*, 2014, **270**, 403–410.
52 Y. Wu, S. W. Cui, J. Wu, L. Ai, Q. Wang and J. Tang, *Carbohydr. Polym.*, 2012, **88**, 926–930.
53 Y. Wu, S. W. Cui, J. Tang and X. Gu, *Food Chem.*, 2007, **105**, 1599–1605.
54 Y. Wu, S. W. Cui, J. Tang, Q. Wang and X. Gu, *Carbohydr. Polym.*, 2007, **70**, 437–443.
55 Z.-S. Wu, Y. Sun, Y.-Z. Tan, S. Yang, X. Feng and K. Müllen, *J. Am. Chem. Soc.*, 2012, **134**, 19532–19535.
56 A. Bello, F. Barzegar, D. Momodu, J. Dangbegnon, F. Taghizadeh and N. Manyala, *Electrochim. Acta*, 2015, **151**, 386–392.
57 S. L. Rebelo, A. Guedes, M. E. Szefczyk, A. M. Pereira, J. P. Araujo and C. Freire, *Phys. Chem. Chem. Phys.*, 2016, **18**, 12784–12796.
58 Z. Yang, J. Ren, Z. Zhang, X. Chen, G. Guan, L. Qiu, Y. Zhang and H. Peng, *Chem. Rev.*, 2015, **115**, 5159–5223.
59 P. Kleszyk, P. Ratajczak, P. Skowron, J. Jagiello, Q. Abbas, E. Frąckowiak and F. Béguin, *Carbon*, 2015, **81**, 148–157.
60 G. A. Ferrero, A. B. Fuertes and M. Sevilla, *Sci. Rep.*, 2015, **5**, 16618.
61 L. Zhao, L. Z. Fan, M. Q. Zhou, H. Guan, S. Qiao, M. Antonietti and M. M. Titirici, *Adv. Mater.*, 2010, **22**, 5202–5206.
62 D.-W. Wang, F. Li, Z.-G. Chen, G. Q. Lu and H.-M. Cheng, *Chem. Mater.*, 2008, **20**, 7195–7200.
63 S. Kondrat, C. R. Pérez, V. Presser, Y. Gogotsi and A. A. Kornyshev, *Energy Environ. Sci.*, 2012, **5**, 6474.
64 C. Largeot, C. Portet, J. Chmiola, P.-L. Taberna, Y. Gogotsi and P. Simon, *J. Am. Chem. Soc.*, 2008, **130**, 2730–2731.
65 J. Chmiola, G. Yushin, Y. Gogotsi, C. Portet, P. Simon and P. L. Taberna, *Science*, 2006, **313**, 1760–1763.
66 J.-W. Jeon, R. Sharma, P. Meduri, B. W. Arey, H. T. Schaef, J. L. Lutkenhaus, J. P. Lemmon, P. K. Thallapally, M. I. Nandasiri, B. P. McGrail and S. K. Nune, *ACS Appl. Mater. Interfaces*, 2014, **6**, 7214–7222.
67 D. Y. Chung, K. J. Lee, S.-H. Yu, M. Kim, S. Y. Lee, O.-H. Kim, H.-J. Park and Y.-E. Sung, *Adv. Energy Mater.*, 2015, **5**, 1401309.
68 C. Peng, J. Lang, S. Xu and X. Wang, *RSC Adv.*, 2014, **4**, 54662–54667.
69 Y. Li and M. Cao, *Chem.–Asian J.*, 2015, **10**, 1496–1504.
70 T. Zhu, J. Zhou, Z. Li, S. Li, W. Si and S. Zhuo, *J. Mater. Chem. A*, 2014, **2**, 12545.
71 S. Yu, H. Wang, C. Hu, Q. Zhu, N. Qiao and B. Xu, *J. Mater. Chem. A*, 2016, **4**, 16341–16348.
72 B. Xu, H. Duan, M. Chu, G. Cao and Y. Yang, *J. Mater. Chem. A*, 2013, **1**, 4565.
73 B. Xu, S. Hou, G. Cao, F. Wu and Y. Yang, *J. Mater. Chem.*, 2012, **22**, 19088.
74 M. Sevilla and R. Mokaya, *Energy Environ. Sci.*, 2014, **7**, 1250.